Figures of Chapter 3

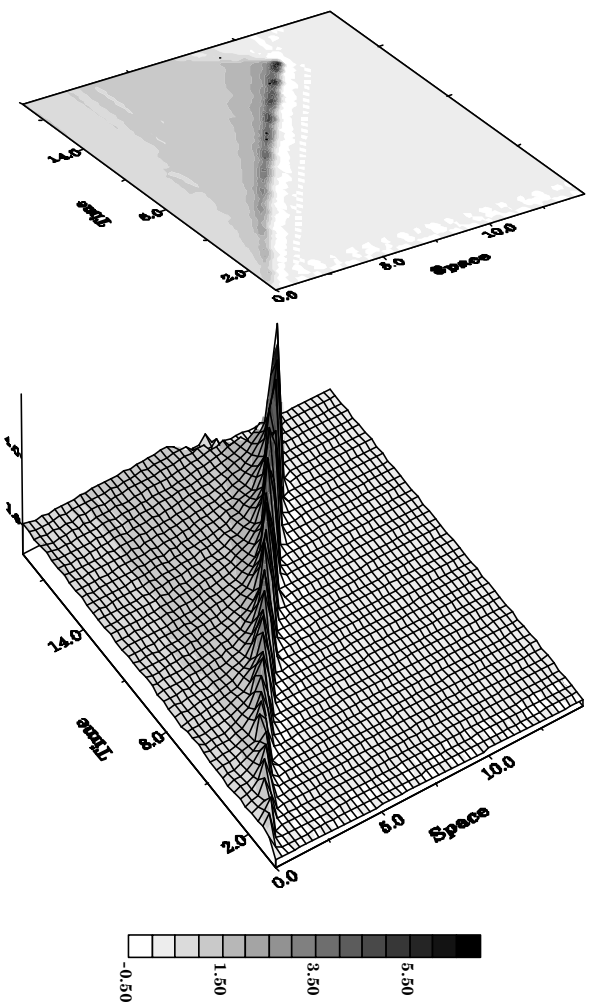

(a)

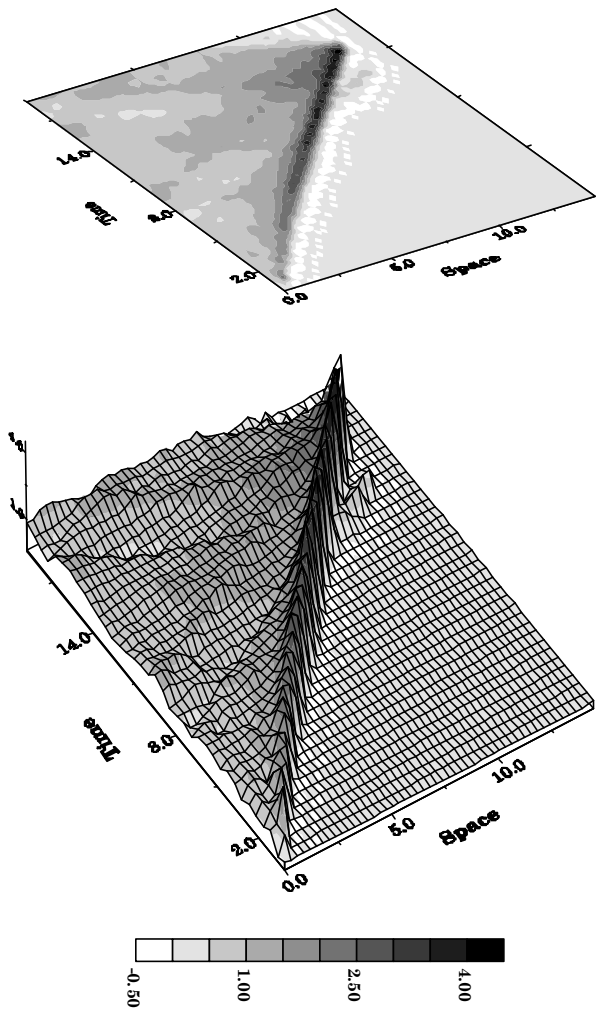

(b)

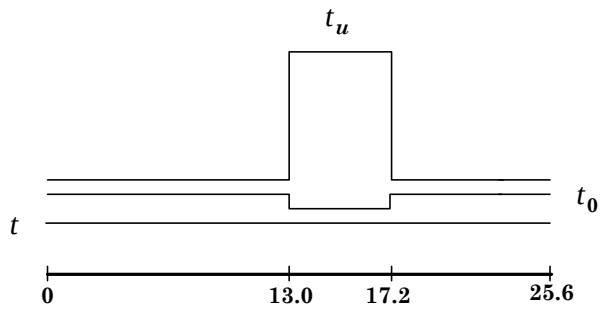

Figure 3.1. Slip velocity behavior for of a heterogeneous model of the strength S, which reproduces a barrier–healing phase. Both in the BIE (a) and in the FD (b) case t_0 = 1 and t_u = 1.8 everywhere, except that in the area $13 \leq x_1 \leq 17.2$, where $t_0 = 0.1$ and $t_u = 11$. The parameters t_f and d_0 are uniform and they are 0 and 2.094 respectively. The solutions are plotted in a portion of the entire fault length in order to emphasize the arrest process. In the lower part of the figure we have represented in a schematic draw the distribution of constitutive parameters along the fault line.

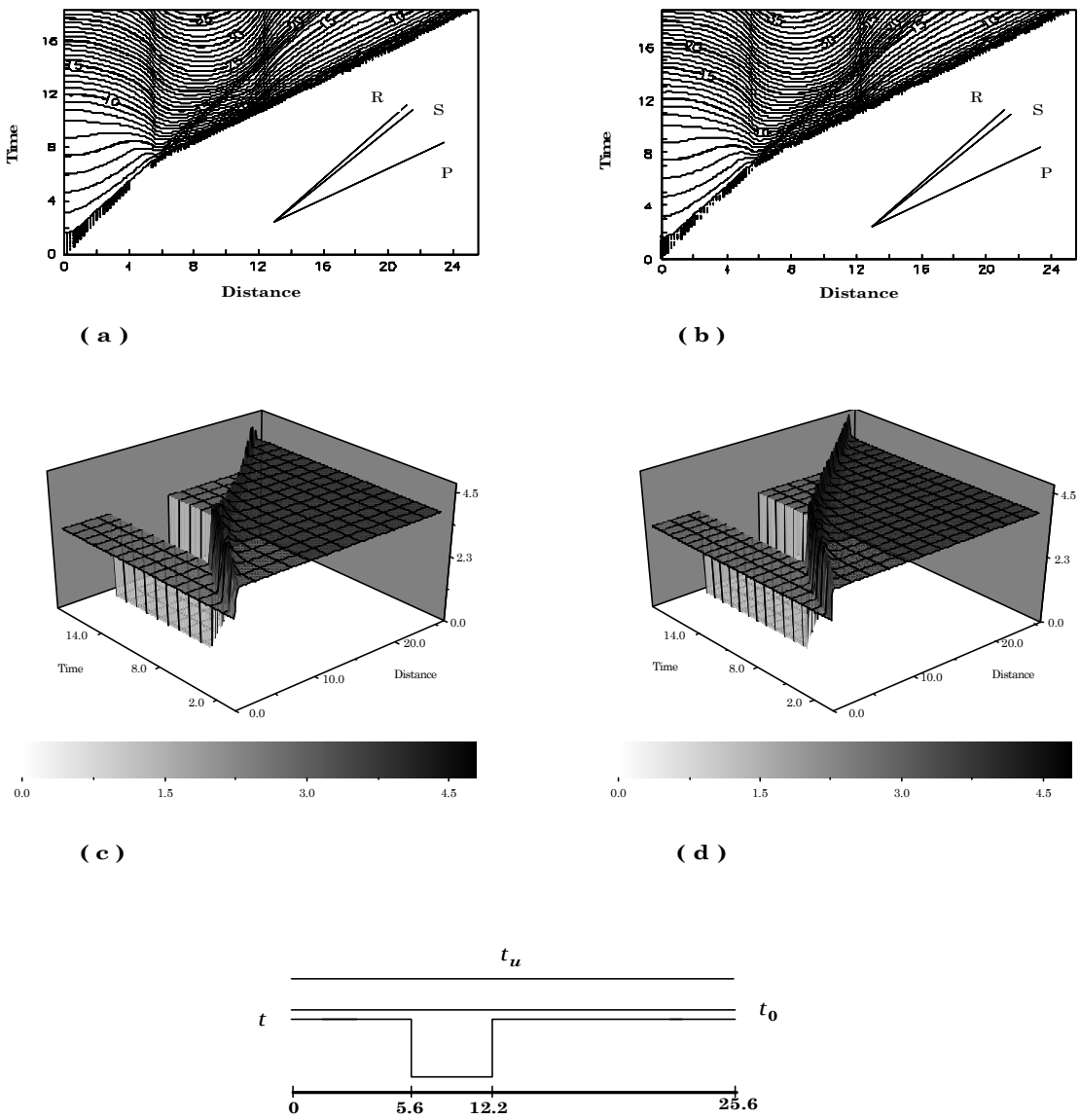

Figure 3.2. Normalized slip obtained in a configuration in which only t_f is heterogeneous: t_u = 3 everywhere, except that in 5.6 $\leq x_1 \leq$ 12, where it is 0. Other parameters are t_0 = 4, t_u = 4.8 and d_0 = 1.309. (a) BIE case, (b) FD case. As well as in the Figure 6, the position of the heterogeneity is depicted in the scheme in the lower part of the figure.

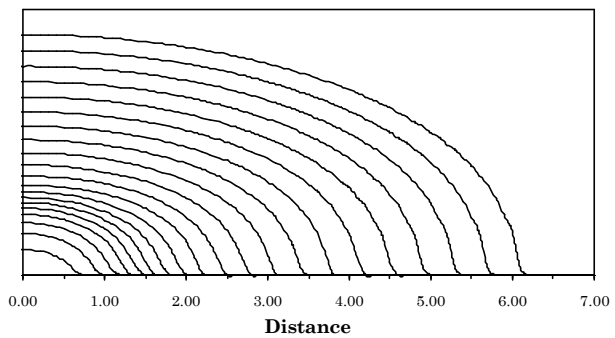

(a)

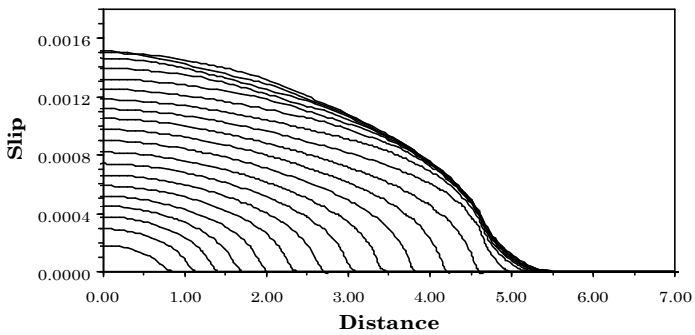

(b)

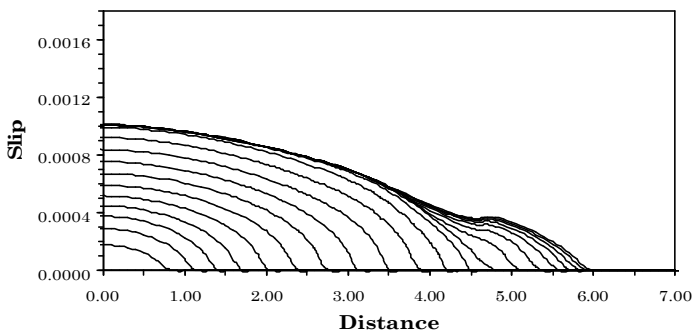

(c)

Figure 3.3. Slip behavior vs. position along the fault line at different time steps (each line is a slip snapshot). (a) Reference omogeneous case, representing a classical velocity weakening rheology ($a = 0.012$, $b = 0.016$, $L = 1 \cdot 10^{-5}\ m$). In the barrier – healing case (b) the parameters a and b are homogeneous along the entire fault line, and equal to those of reference case (a), but $L = 1 \cdot 10^{-2}\ m$ after $x_1 = 5\ m$. In the self – healing configuration (c), on the contrary, L is uniform along the fault, but after $x_1 = 5\ m$ the rheology is velocity strengthening ($a = 0.015$, $b = 0.012$). The scale of abscissa is the same in three cases, and values are expressed in meters, as well as the slip values.

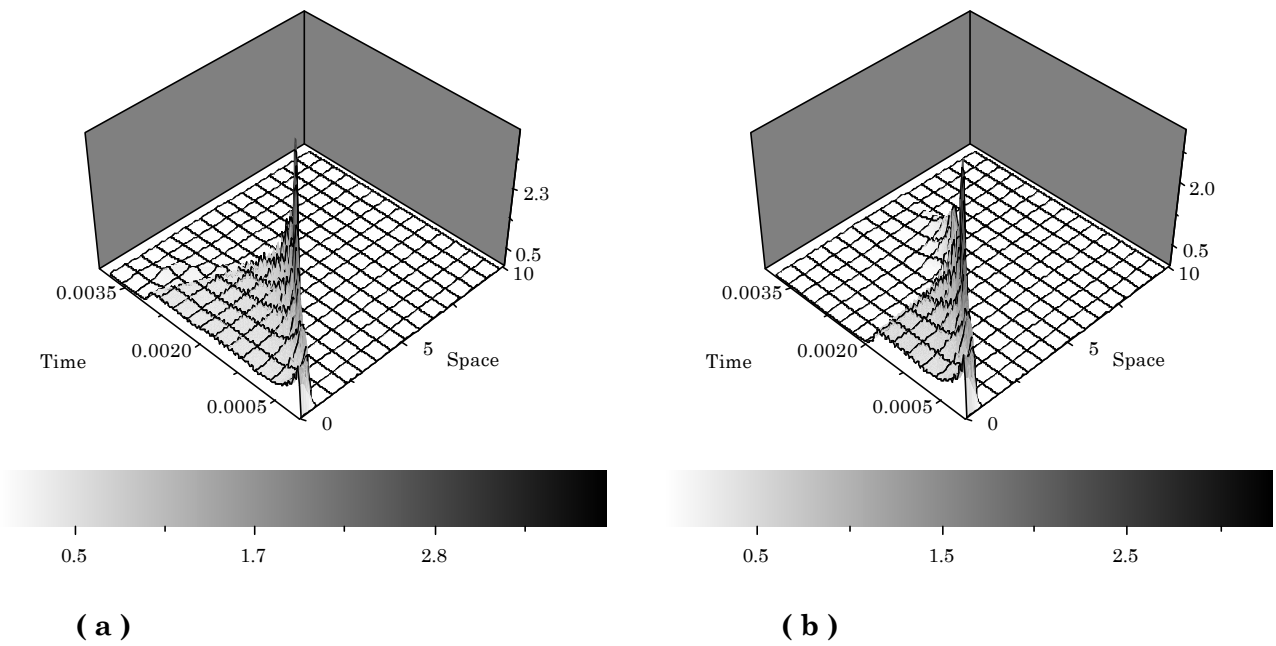

(a) **(b)**

Figure 3.4. 3 – D views of slip velocity in the heterogeneous configurations described in Figure 3.3b and c: barrier – healing case (a) and self–healing one (c).

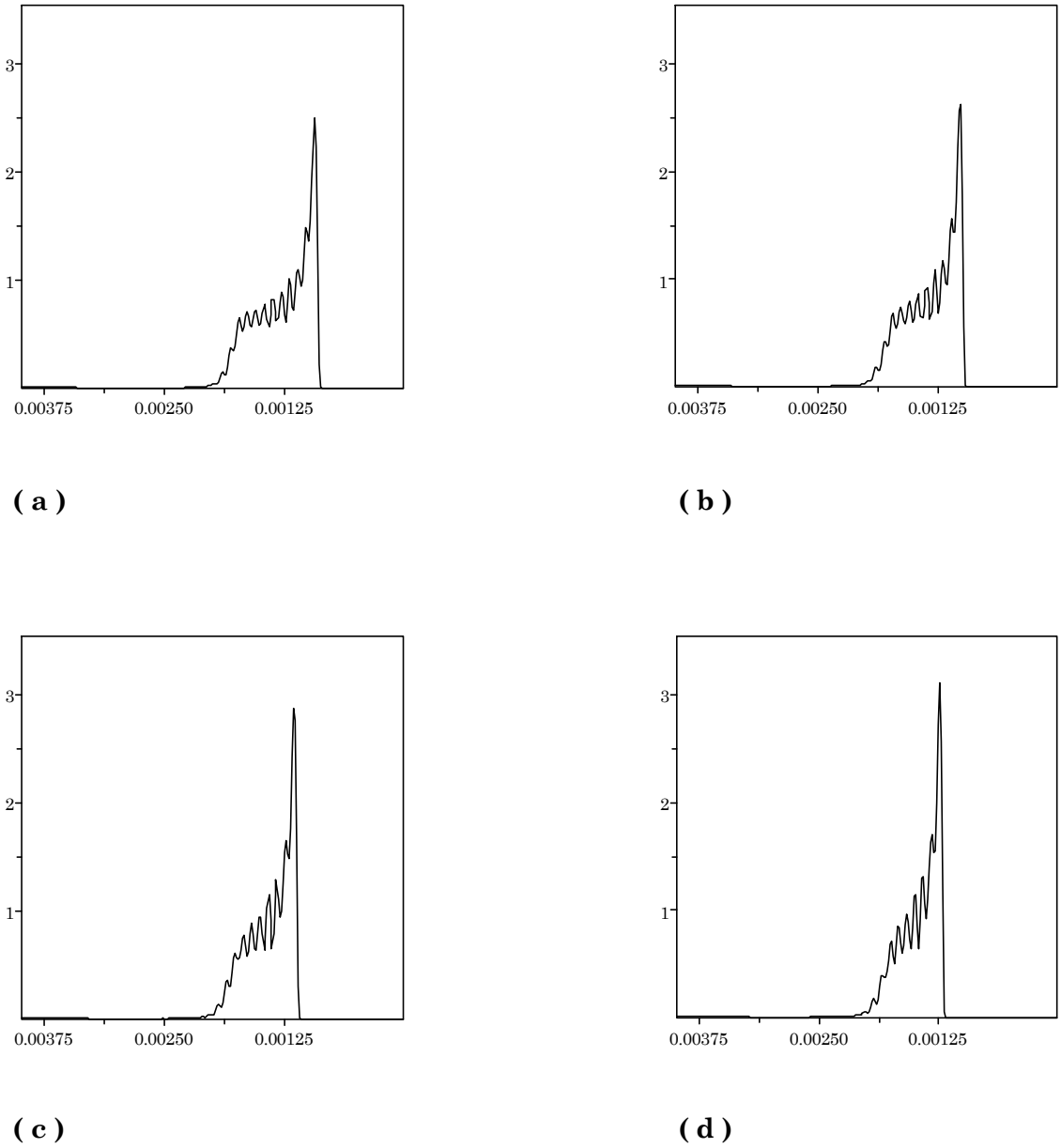

Figure 3.5. Slip duration in the self–healing case, in different fault points: (a) slip velocity versus time in $x_1 = 2.2$, (b) $x_1 = 2.4$, (c) $x_1 = 2.7$, (d) $x_1 = 2.9$.

A)

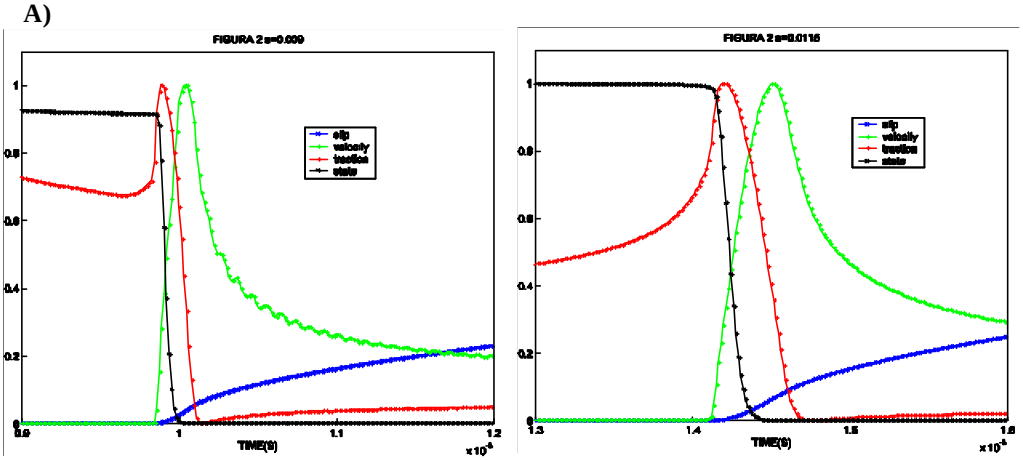

B)

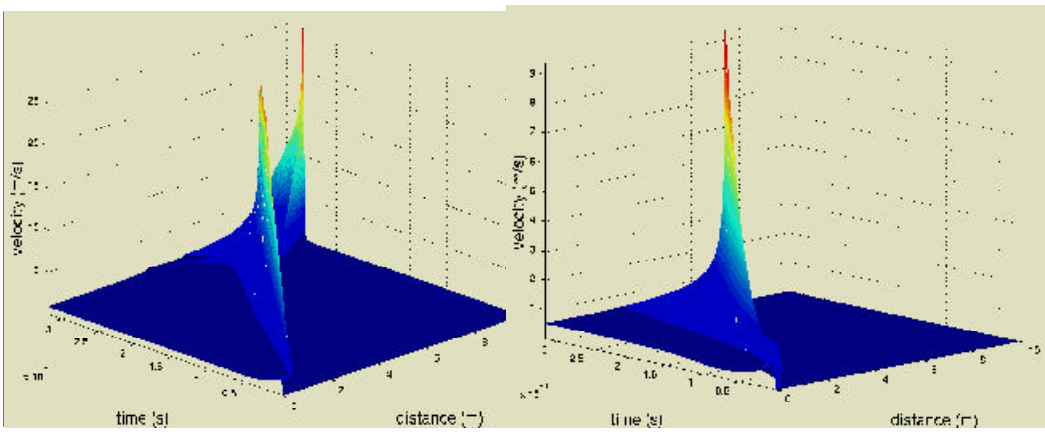

Figure 3.6. Time histories of relevant physical quantities (a) and spatio-temporal evolution of slip velocity (b) for two simulations performed with different values of the parameter a controlling the direct effect of friction in the governing equation for friction. A slowness evolution law is used. Smaller values of the parameter a yields higher rupture velocities (the rupture front bifurcation occurs only in the simulation with the smaller value).

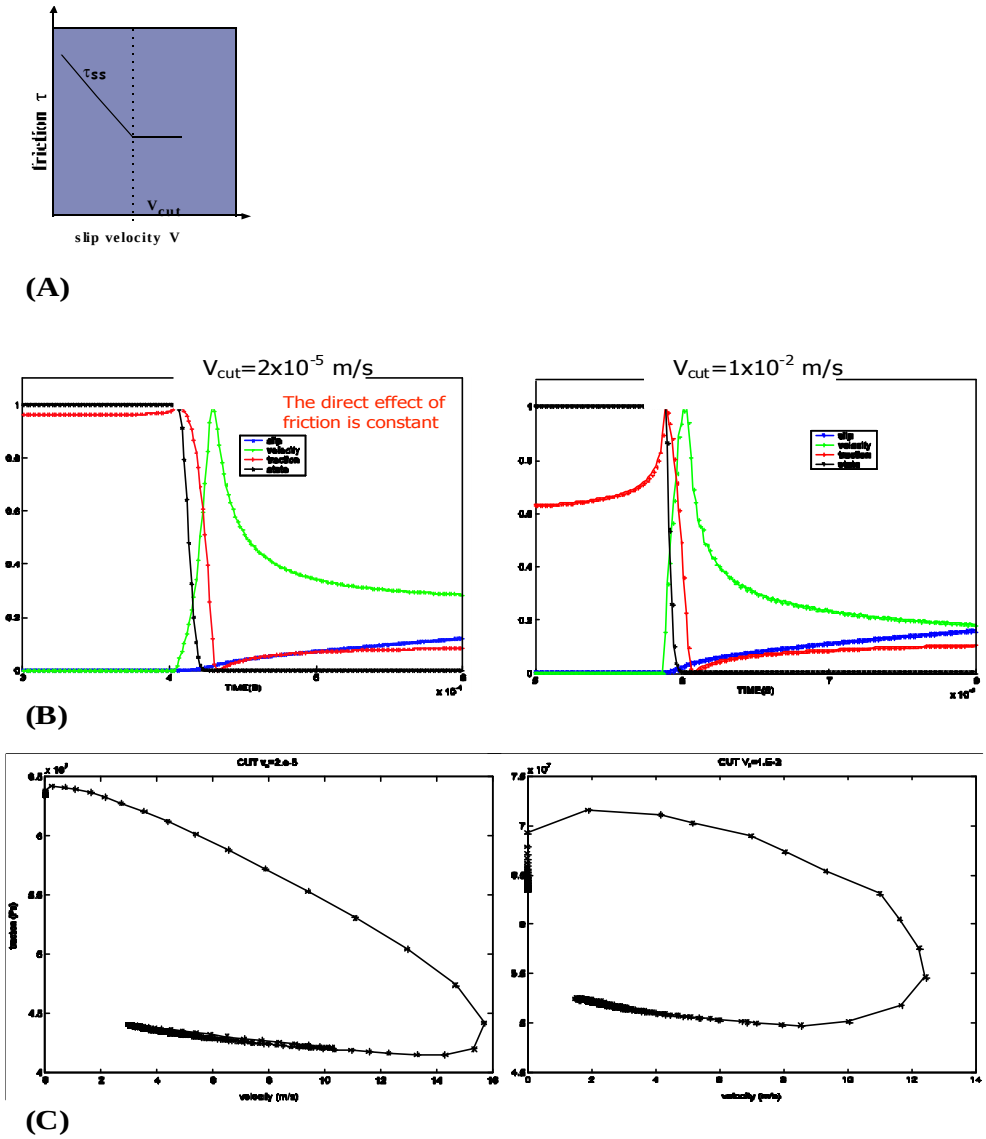

Figure 3.7. Top panel (a) illustrates the adopted modification of friction behavior as a function of slip velocity for the steady-state traction. We assume that in the governing equation the direct effect of friction is constant and independent of slip velocity for V >V_{cut}, as explained in the text. (b) and (c) show the time histories of relevant physical quantities and the phase diagrams, respectively, calculated for two simulations performed using a slowness evolution law (1) with different values of V_{cut}. Left panels refer to a value which is only twice the initial velocity (the direct effect of friction is always independent of slip velocity during most of the simulation); while the right panels show the time histories and the phase diagram for a quite larger velocity cutoff.

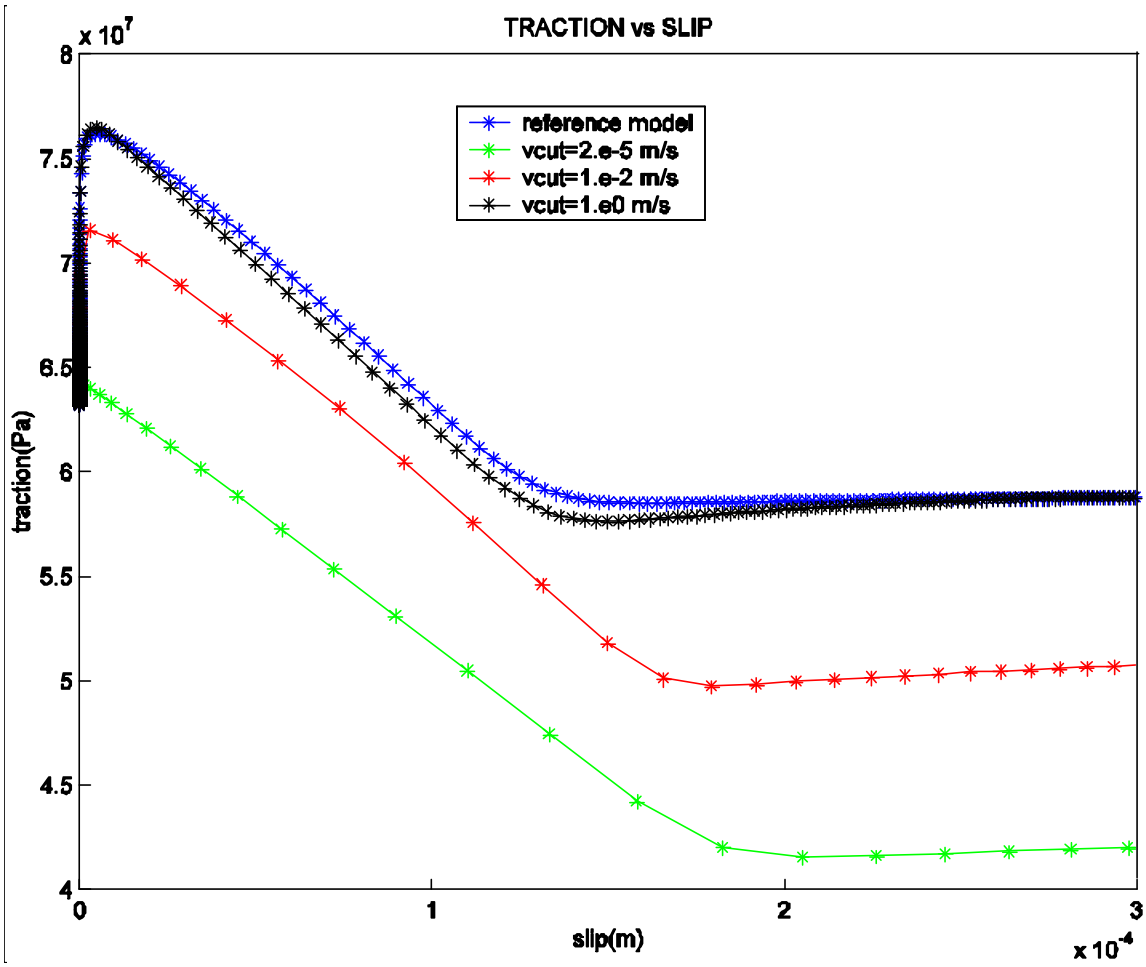

Figure 3.8. SW curves calculated from several simulations performed using a slowness law and different values of the slip rate cutoff (V_{cut}). The SW curve of the reference model is included for comparison.

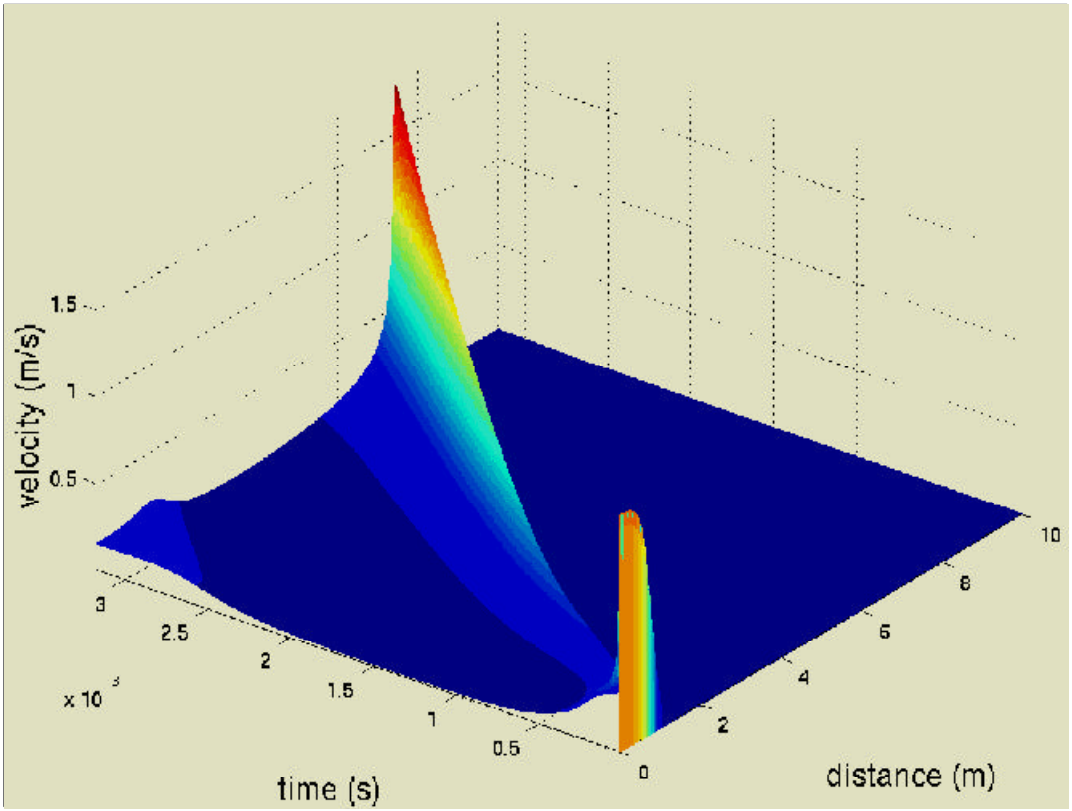

Figure 3.9. Spatio-temporal evolution of slip velocity from a simulation performed using the constitutive law proposed by Perrin et al. (1995) and stated in (3.2). The nucleation patch is shown by the larger initial slip rate. The reference slip velocity V_* in this simulation is equal to 10 m/s and the low velocity cutoff V_P in (3.2) is 10^{-2} m/s. The solution shows healing of slip. The rapid restrengthening is so fast that the nucleation patch undergoes to an aseismic slip episode during the considered time window.

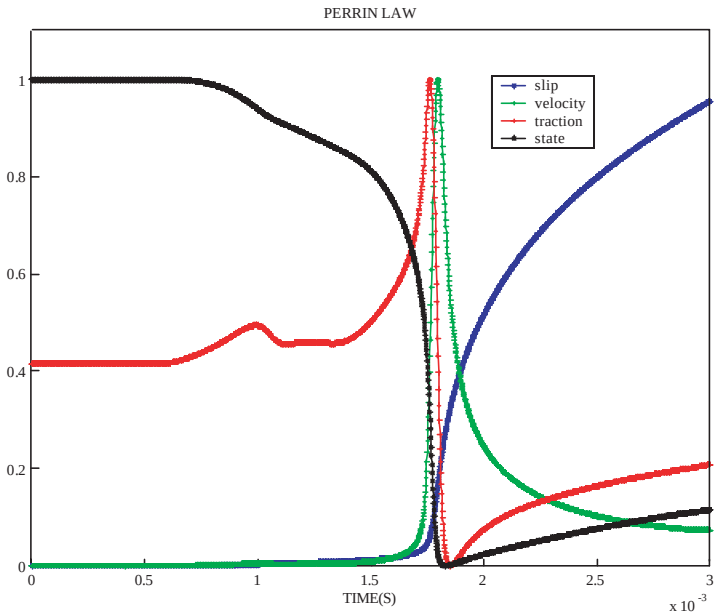

Figure 3.10. Time histories of slip, slip velocity, state variable and total dynamic traction calculated with the constitutive law described in (3.2).

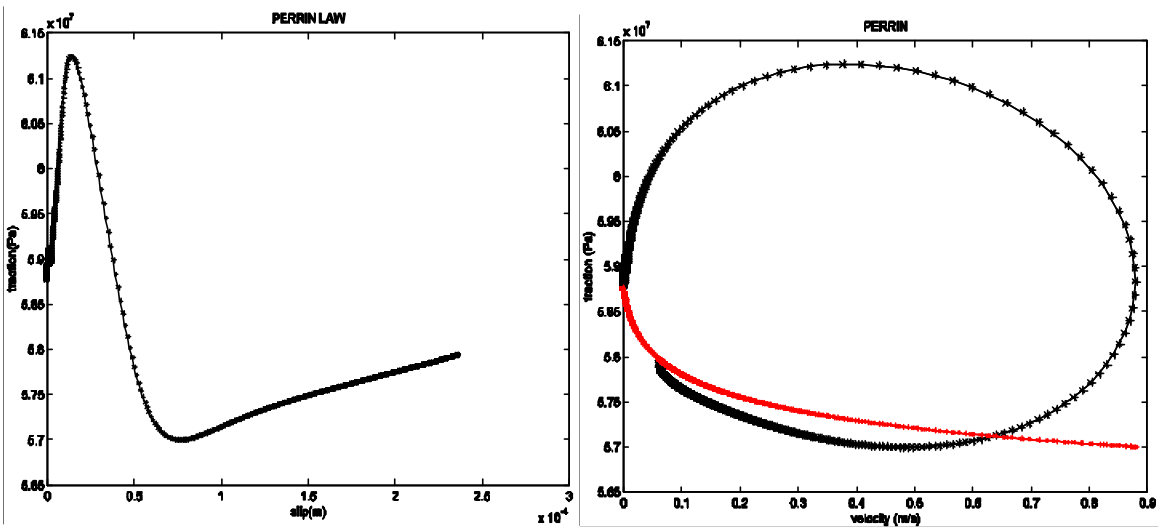

Figure 3.11. SW curve and phase diagram resulting from the simulations performed with the constitutive law described in (3.2). The red curve shows the steady state friction as a function of slip velocity. The straight dot-dashed line represents the radiation-damping curve.

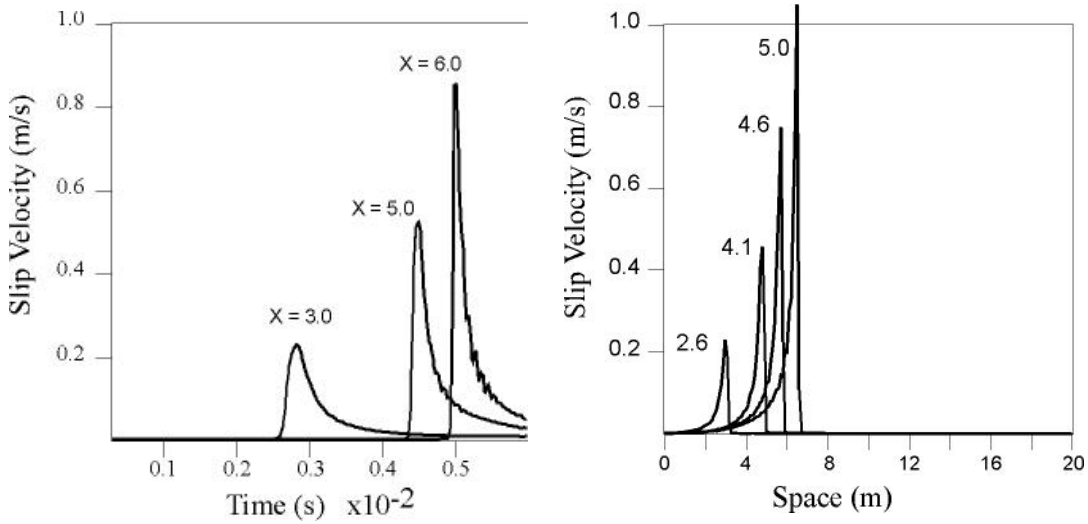

(b) (c)

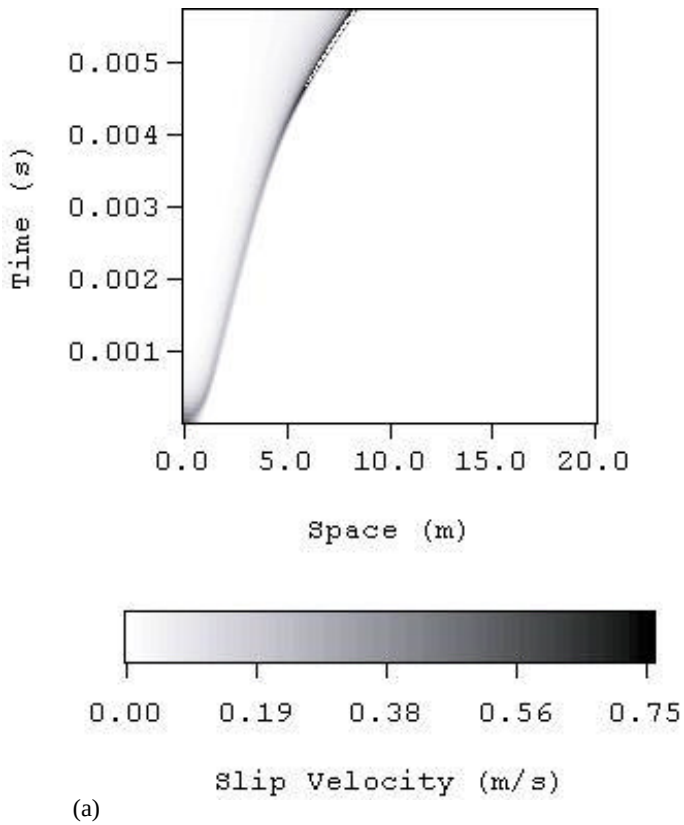

(a)

Figure 3.12. Spatio-temporal evolution (a) and time histories (b) of slip velocity calculated for a simulation performed using the constitutive law described in (3.3). The stars indicate the position along the fault at which the slip velocities are computed.

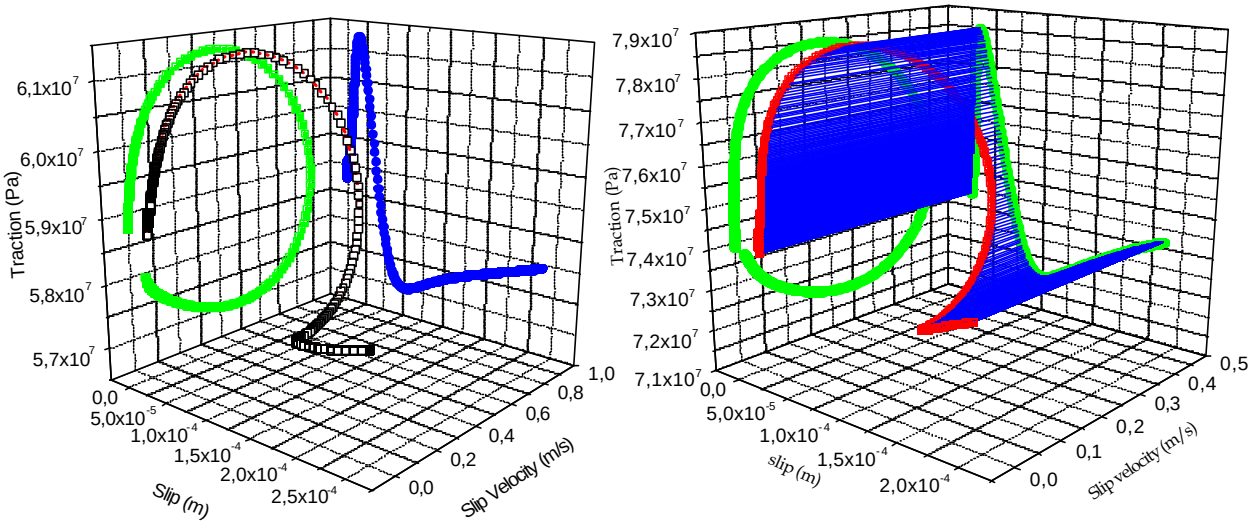

Figure 3.13. Comparison between the 3 - D phase trajectories resulting from the simulations performed with the constitutive laws described in (7) (top panel – a -) and (3.3) (bottom panel - b -) and showing total dynamic traction as a function of slip and slip velocity.

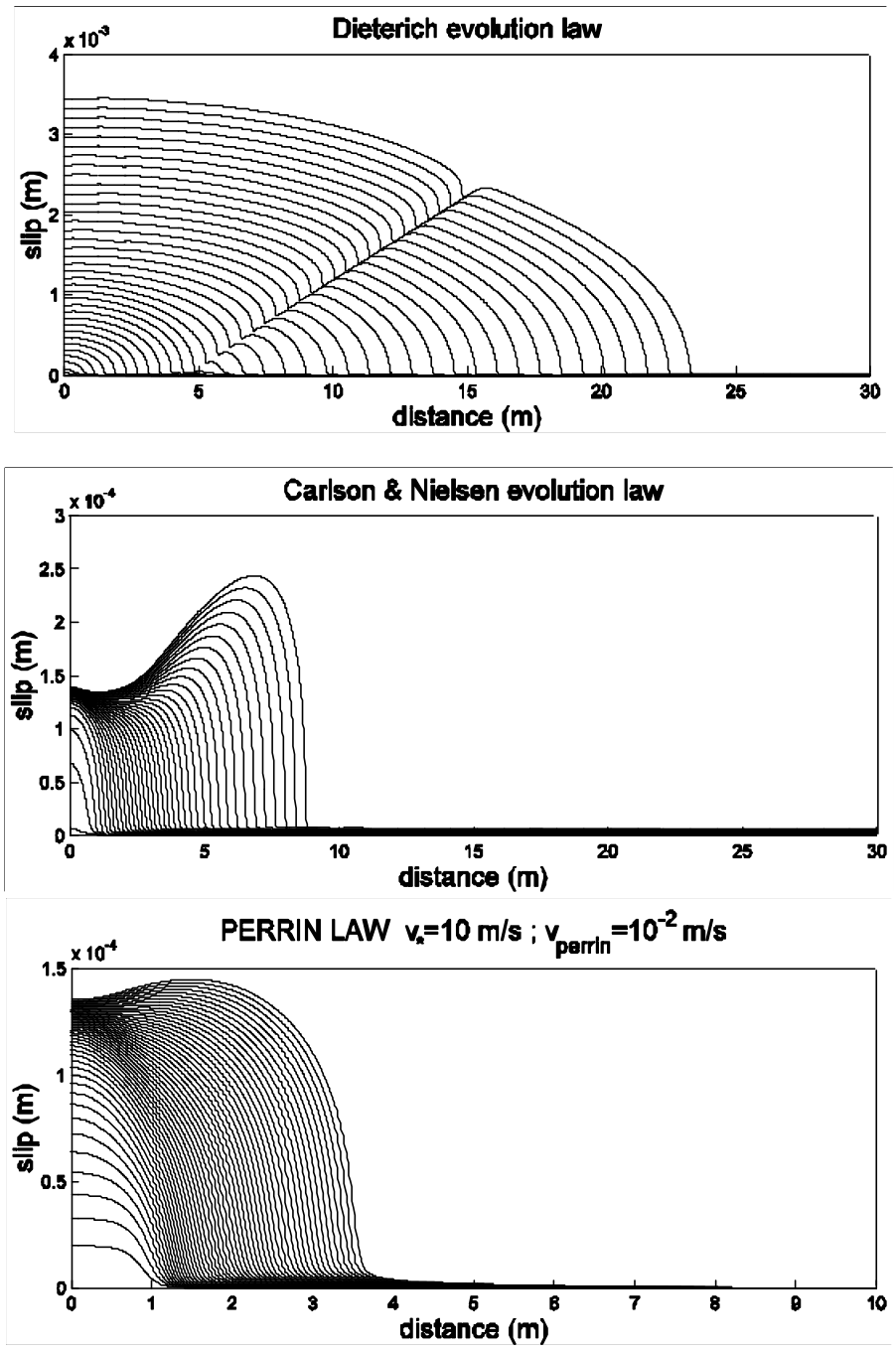

Figure 3.14. Comparison between the slip profiles, obtained by the superposition of snapshots at different time steps of slip along the fault line, resulting from simulations performed with a slowness evolution law (top panel) and with the evolution laws described in (3.2), middle panel, and (3.3) bottom panel.